A rechargeable calcium–oxygen battery that operates at room temperature

https://doi.org/10.1038/s41586-023-06949-x

Received: 18 April 2022

Accepted: 6 December 2023

Lei Ye[1,6], Meng Liao[1,6], Kun Zhang[1,6], Mengting Zheng[2], Yi Jiang[1], Xiangran Cheng[1], Chuang Wang[1], Qiuchen Xu[3], Chengqiang Tang[1], Pengzhou Li[1], Yunzhou Wen[1], Yifei Xu[1], Xuemei Sun[1], Peining Chen[1], Hao Sun[3], Yue Gao[1], Ye Zhang[1], Bingjie Wang[1]✉, Jun Lu[2]✉, Haoshen Zhou[4]✉, Yonggang Wang[5]✉, Yongyao Xia[5], Xin Xu[5] & Huisheng Peng[1]✉

Calcium–oxygen (Ca–O_2) batteries can theoretically afford high capacity by the reduction of O_2 to calcium oxide compounds (CaO_x) at low cost[1–5]. Yet, a rechargeable Ca–O_2 battery that operates at room temperature has not been achieved because the CaO_x/O_2 chemistry typically involves inert discharge products and few electrolytes can accommodate both a highly reductive Ca metal anode and O_2. Here we report a Ca–O_2 battery that is rechargeable for 700 cycles at room temperature. Our battery relies on a highly reversible two-electron redox to form chemically reactive calcium peroxide (CaO_2) as the discharge product. Using a durable ionic liquid-based electrolyte, this two-electron reaction is enabled by the facilitated Ca plating–stripping in the Ca metal anode at room temperature and improved CaO_2/O_2 redox in the air cathode. We show the proposed Ca–O_2 battery is stable in air and can be made into flexible fibres that are weaved into textile batteries for next-generation wearable systems.

Rechargeable divalent metal batteries using earth-abundant metals are expected to be cheaper and safer than lithium (Li)-ion batteries[4–9]. Among divalent metals, calcium (Ca) is the most abundant (41,500 ppm by mass) in the crust of Earth compared with magnesium (Mg; 23,300 ppm) and zinc (Zn; 70 ppm), and it is more than 2,500 times more abundant than Li (20 ppm) (ref. 10). Furthermore, Ca has a large anode capacity (2,073 mAh cm^{-3}) and low reduction potential (−2.87 V compared with standard hydrogen electrode, V_{SHE}) close to that of Li (−3.04 V_{SHE}), making the cell voltage and energy density of Ca batteries potentially comparable with Li-ion batteries. However, Ca metal tends to react with the electrolyte and form an ionically insulating layer that inhibits the Ca plating–stripping[6,11,12]. The large effective ionic radius (1.0 Å) of divalent calcium ions (Ca^{2+}) also leads to the difficult Ca^{2+} (de)intercalation in electrodes and sluggish Ca^{2+} transport at electrode–electrolyte interfaces[13]. Although Ca anodes have been paired with several metal oxide cathodes capable of Ca^{2+} intercalation, these Ca-ion batteries generally have limited capacity (<200 mAh $g_{cathode}^{-1}$) and/or cycling stability (<100 cycles) (refs. 2,5,14,15). Compared with the Ca^{2+}-intercalation mode, Ca batteries relying on conversion redox chemistries are promising to fully use the electrochemical properties of abundant Ca metal.

Among all Ca-based batteries, calcium–oxygen (Ca–O_2) batteries consisting of metallic Ca anode and air cathode would, in principle, have the highest theoretical energy density because the fuel at the air cathode, O_2, is derived from air rather than stored in the battery[16–18]. However, as the key to achieve a usable Ca–O_2 battery, the CaO_x/O_2 chemistry typically has poor electrochemical reversibility at room temperature. Early studies have suggested that Ca–O_2 batteries undergo a four-electron reaction involving the thermodynamically difficult cleavage remake of O–O bonds for calcium oxide (CaO) formation decomposition and could be examined only at elevated temperatures to overcome the sluggish CaO decomposition in the cathode and Ca plating–stripping in the anode[4,19,20]. The resultant cells are nearly not rechargeable (<10 cycles) at the elevated temperatures, with extremely large cell polarizations originating from inadequate Ca^{2+} transport and parasitic reactions caused by electrolyte instabilities on O_2 and/or Ca metal, not to mention the stable operation at room temperature. Therefore, realizing rechargeable Ca–O_2 batteries with the expected electrochemical performance at room temperature is a challenge.

We demonstrate that, by using an ionic liquid-based electrolyte that enables both reversible Ca plating–stripping and improved Ca^{2+} kinetics, a two-electron transfer reaction pathway based on CaO_2/O_2 redox can lead to a rechargeable Ca–O_2 battery at room temperature, with chemically reactive calcium peroxide (CaO_2) as the main discharge product. We used Ca metal as the anode and aligned carbon nanotube (CNT) sheet as the air cathode (Fig. 1a). Our electrolyte is 0.5 M calcium bis(trifluoromethanesulphonimide) ($Ca(TFSI)_2$) dissolved in a 1:1 volume mixture of ionic liquid 1-ethyl-3-methylimidazolium tetrafluoroborate (EMIM-BF_4) and dimethyl sulphoxide (DMSO). We chose $Ca(TFSI)_2$ as the salt because it is commercially available and

---

[1] State Key Laboratory of Molecular Engineering of Polymers, Department of Macromolecular Science, Institute of Fiber Materials and Devices, and Laboratory of Advanced Materials, Fudan University, Shanghai, China. [2] College of Chemical and Biological Engineering, Zhejiang University, Hangzhou, China. [3] Frontiers Science Center for Transformative Molecules, Shanghai Jiao Tong University, Shanghai, China. [4] Center of Energy Storage Materials and Technology, College of Engineering and Applied Sciences, Jiangsu Key Laboratory of Artificial Functional Materials, National Laboratory of Solid-State Microstructures and Collaborative Innovation Center of Advanced Microstructures, Nanjing University, Nanjing, China. [5] Department of Chemistry and Shanghai Key Laboratory of Molecular Catalysis and Innovative Materials, Institute of New Energy, iChEM (Collaborative Innovation Center of Chemistry for Energy Materials), Fudan University, Shanghai, China. [6] These authors contributed equally: Lei Ye, Meng Liao, Kun Zhang. ✉e-mail: wangbingjie@fudan.edu.cn; junzoelu@zju.edu.cn; hszhou@nju.edu.cn; ygwang@fudan.edu.cn; penghs@fudan.edu.cn

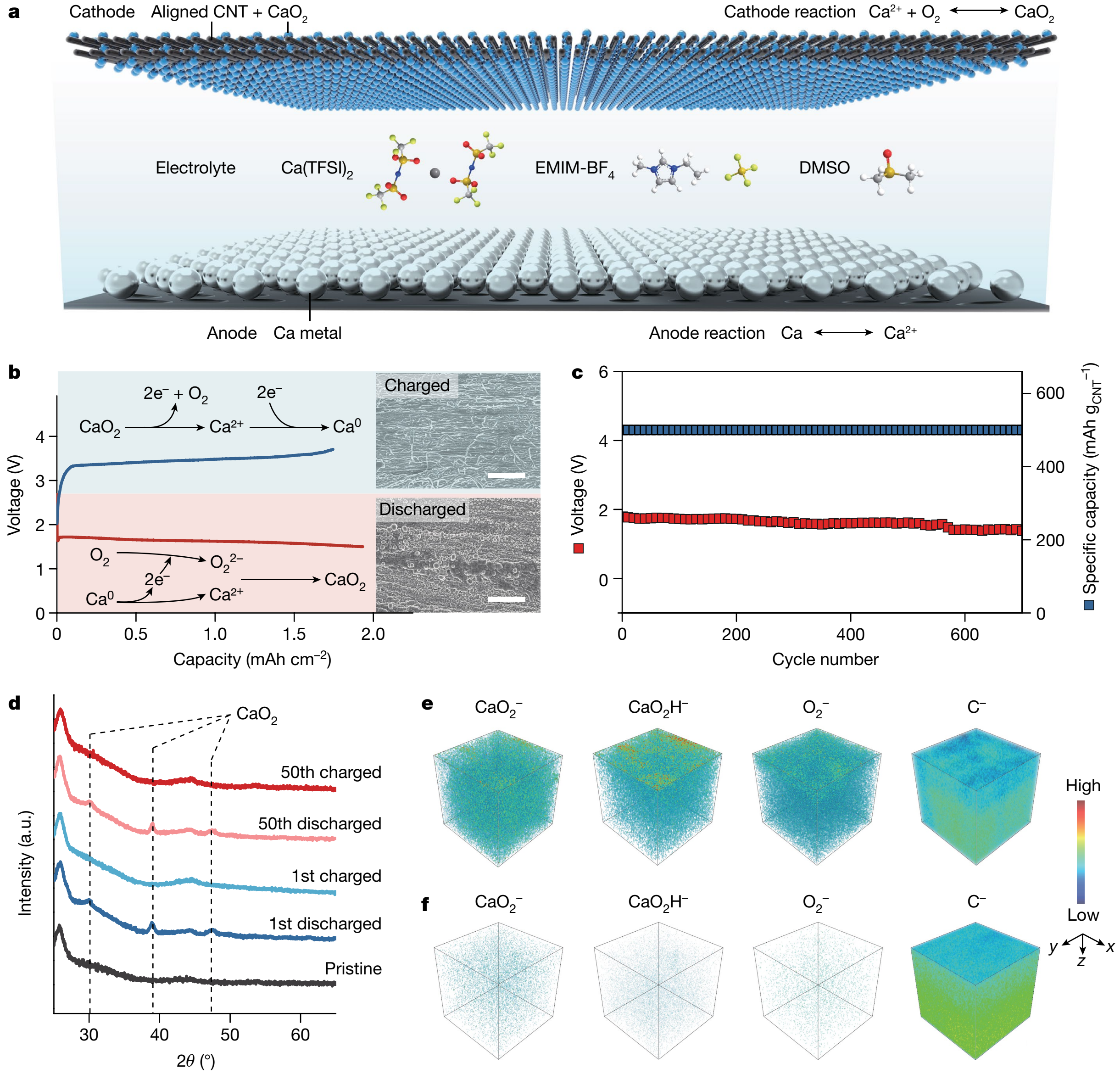

Fig. 1 | Rechargeable Ca–O$_2$ batteries at room temperature with CaO$_2$ as the main discharge product. **a**, Schematic of the rechargeable Ca–O$_2$ battery, with an aligned CNT sheet as cathode, Ca metal as anode and 0.5 M Ca(TFSI)$_2$ in EMIM-BF$_4$/DMSO (50:50 vol%) as electrolyte. On the cathode side, O$_2$ is reduced and combined with Ca^{2+} in the electrolyte to form CaO$_2$ during discharge, and the reverse reaction occurs during charge. On the anode side, metallic Ca is stripped during discharge and re-plated on recharge. **b**, Deep discharge–charge curves of the Ca–O$_2$ battery. The battery was discharged to 1.5 V and then recharged to 3.7 V at a current density of 1 A g^{-1}. Inset, a flow diagram of the proposed reaction pathway for the Ca–O$_2$ battery during discharge (red) and charge (blue). Scanning electron microscopy (SEM) images of the aligned CNT cathode show that spherical CaO$_2$ particles after discharging to 1.5 V (bottom) disappear after charging to 3.7 V (top). Scale bar, 2 μm (top and bottom). **c**, Discharge plateau of the Ca–O$_2$ battery is steady over 700 cycles at a current density of 1 A g^{-1} and a specific capacity of 500 mAh g^{-1}. **d**, XRD patterns of the pristine aligned CNT cathode and the discharged–charged cathodes after the first and 50th cycles. **e**, Three-dimensional distributions of ^{72}CaO$_2^-$, ^{73}CaO$_2$H$^-$, ^{32}O$_2^-$ and ^{12}C$^-$ constructed based on a TOF-SIMS depth scan of the discharged cathode showing the presence and uniform distribution of CaO$_2$. The analysis area was 50 × 50 μm^2. **f**, Three-dimensional distributions of ^{72}CaO$_2^-$, ^{73}CaO$_2$H$^-$, ^{32}O$_2^-$ and ^{12}C$^-$ constructed based on a TOF-SIMS depth scan of the recharged cathode showing the full decomposition of CaO$_2$. The analysis area was 50 × 50 μm^2. a.u., arbitrary units.

TFSI$^-$ is known to induce fluoride-rich solid-electrolyte interphase (SEI) for reversible metal anodes[4,21,22]. Ionic liquid EMIM-BF$_4$ is used to widen the voltage window and DMSO is introduced to enhance the diffusivity of Ca^{2+} and O$_2$ for the resultant electrolyte[23]. The aligned CNT sheet enables us to focus solely on the cathode reaction mechanism because it can be used directly without additional binder, conductive agent and/or catalyst[24] (Extended Data Fig. 1a–c). When the as-made battery was discharged, particles (diameters of about 100 nm) of the discharge product formed on the aligned CNT sheet, which were then fully decomposed on charge processes (Fig. 1b). The Ca–O$_2$ batteries can operate at room temperature for more than 700 cycles, at a current density of 1 A g$_{CNT}^{-1}$ (0.1 mA cm^{-2}) and a limited specific capacity of 500 mAh g$_{CNT}^{-1}$, with a flat voltage plateau at about 1.7 V (Fig. 1c and Extended Data Fig. 1d). Other Ca–O$_2$ batteries measured under various operation conditions and with different cathode mass loadings will be described later in the paper.

Identifying the discharge products in our developed Ca–O$_2$ batteries has important implications for understanding the O$_2$ reduction mechanism. The main discharge product was first indicated to be CaO$_2$ by powder X-ray diffraction (XRD; Fig. 1d and Extended Data Fig. 2a),

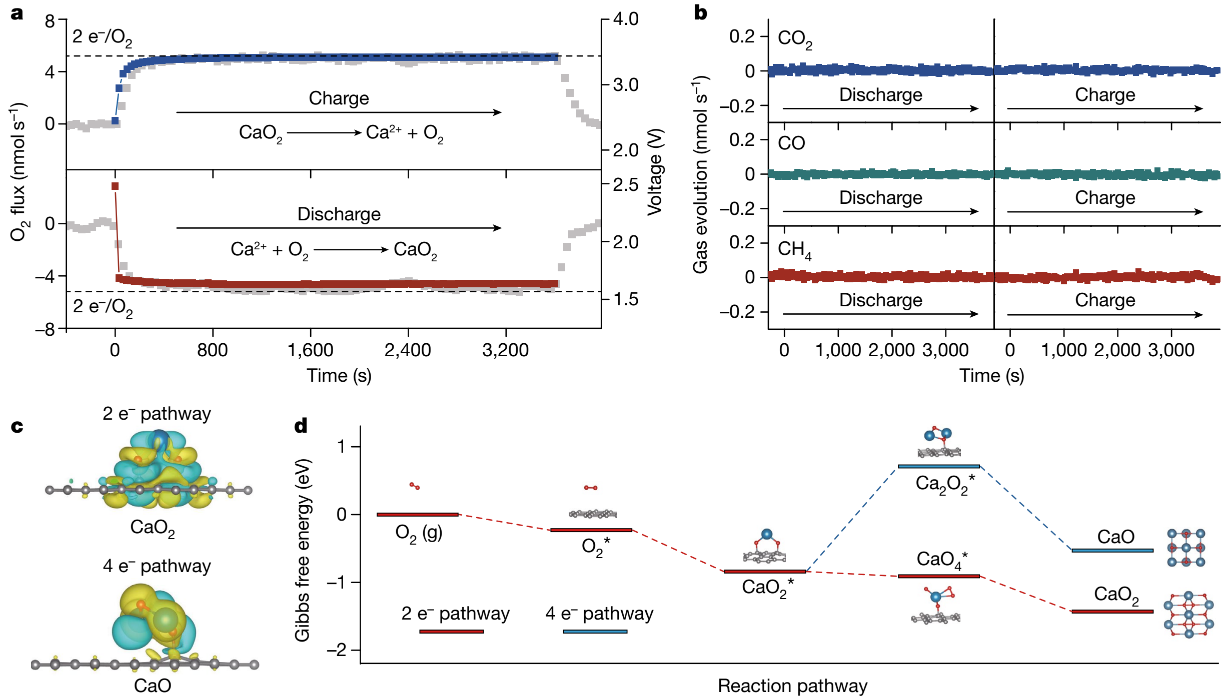

Fig. 2 | Cathode reaction of Ca–O_2 batteries involves reversible two-electron O_2/CaO_2 chemistry. a, DEMS profiles of the Ca–O_2 battery showing O_2 consumption during discharging and O_2 evolution during charging at a current density of 1 A g^{-1}. **b**, DEMS profiles of the Ca–O_2 battery showing that the signatures of electrolyte decomposition (CO_2, CO and CH_4) during CaO_2 formation and decomposition are all below 0.05 nmol s^{-1}. **c**, Differential charge density distributions of CaO_2-adsorbed (top) and CaO-adsorbed (bottom) CNT cathodes. Intensive electron transfer occurs from CNT to CaO_2. Blue and yellow regions represent charge depletion and accumulation regions, respectively. **d**, The calculated Gibbs free energy of O_2 reduction on the CNT cathode is lower for the two-electron pathway (red) and, therefore, the two-electron pathway is more thermodynamically and kinetically favourable than the four-electron pathway (blue).

with main peaks at 30.1° and 38.9° corresponding to the (101) and (110) reflections of CaO_2 crystals, respectively. This result is in line with the selected area electron diffraction pattern (Extended Data Fig. 2b). On charging, the characteristic peaks of CaO_2 disappeared, implying reversible oxidation of the CaO_2 discharge product. This trend is similar to that in the subsequent cycles (for example, 50 cycles; Fig. 1d), which suggests the reversibility of the battery reaction. Furthermore, time-of-flight secondary ion mass spectrometry (TOF-SIMS) depth profiling of the discharged sample showed three-dimensional distributions of CaO_2^- ($m/z = 72$), CaO_2H^- ($m/z = 73$), and O_2^- ($m/z = 32$) secondary ions, which are signatures of CaO_2 (Fig. 1e and Extended Data Fig. 2c,d). The polarized distribution of the C^- signal that distinguished the CNT network from the discharge product (CaO_2) indicated that the porous structure of the CNT air cathode was fully used on discharging[25,26]. Notably, in agreement with our XRD results (Fig. 1d), on charging, CaO_2 was fully decomposed to re-expose the CNT cathode, as evidenced by the disappeared secondary ions of CaO_2 in TOF-SIMS depth profiling (Fig. 1f and Extended Data Fig. 2e,f).

We then quantified the cathode reaction using in situ differential electrochemical mass spectrometry (DEMS) at a constant current density of 1 A g^{-1} and a capacity of 1,000 mAh g^{-1} (ref. 27) (Fig. 2a). On discharging, O_2 consumption dominates, with an average electron-to-oxygen (e^-:O_2) ratio of 2.07, consistent with our ultraviolet–visible (UV–vis) spectroscopy-coupled titration results (Extended Data Fig. 3a,b). For the charge process, an average e^-:O_2 ratio of 2.13 was observed, which is quite close to that for the discharge process. This highly reversible e^-:O_2 ratio, together with our discharge product of CaO_2 identified by TOF-SIMS and XRD (Fig. 1d–f and Extended Data Fig. 2), suggests that the discharge process is predominantly based on a two-electron transfer electrochemical reaction ($Ca^{2+} + 2e^- + O_2 \rightarrow CaO_2$; Fig. 1b, inset). This demonstrates the reversible two-electron O_2/CaO_2 chemistry in our Ca–O_2 battery, contrary to the sluggish four-electron transfer reaction thought to occur with Ca–O_2 batteries. Notably, compared with the prominent variation in O_2 (about 5 nmol s^{-1}), nearly no other fluctuations (<0.05 nmol s^{-1}) in potential gaseous by-products, including carbon dioxide (CO_2), carbon monoxide (CO), methane (CH_4) and water (H_2O) were traced in DEMS (Fig. 2b and Extended Data Fig. 3c,d), further confirming the CaO_2 formation–decomposition as the main reaction in our Ca–O_2 batteries.

The two-electron reaction pathway, with CaO_2 as the discharge product, thermodynamically and kinetically favours the reversibility of Ca–O_2 batteries. Differential charge density calculations show that compared with CaO (the discharge product in the four-electron reaction pathway), CaO_2 shows better electron transfer with the carbon-based air cathode (Fig. 2c) and thus suggests the facilitated reduction of O_2. The O_2 reduction pathways through two- and four-electron transfer are then compared using density functional theory calculations (Fig. 2d). The two-electron mechanism exhibits a lower Gibbs free-energy difference ($\Delta G_{CaO_2} = -1.43$ eV) than the four-electron mechanism ($\Delta G_{CaO} = -0.53$ eV) at room temperature, mainly attributed to the absence of O–O bond cleavage in CaO_2 formation. As a reverse reaction, the decomposition of CaO_2 is also feasible at a minimum charging potential of 3.36 V (Extended Data Fig. 3e), consistent with our cycling experiment (Fig. 1b,c). Hence, the 2e^- CaO_2 formation–decomposition paves the way for our electrochemically reversible Ca–O_2 batteries at room temperature.

When the anode disassembled from a recharged Ca–O_2 battery was examined, we found newly deposited microscale, dark-grey Ca (Fig. 3a, inset, and Extended Data Fig. 4a–c). Energy-dispersive X-ray spectroscopy analysis showed the deposits contained a Ca-rich feature (93%) and an average Ca to calcium fluoride (Ca:CaF_2) molar ratio of 13:1 as deduced from the Ca:F ratio (Fig. 3a), preliminarily pointing to

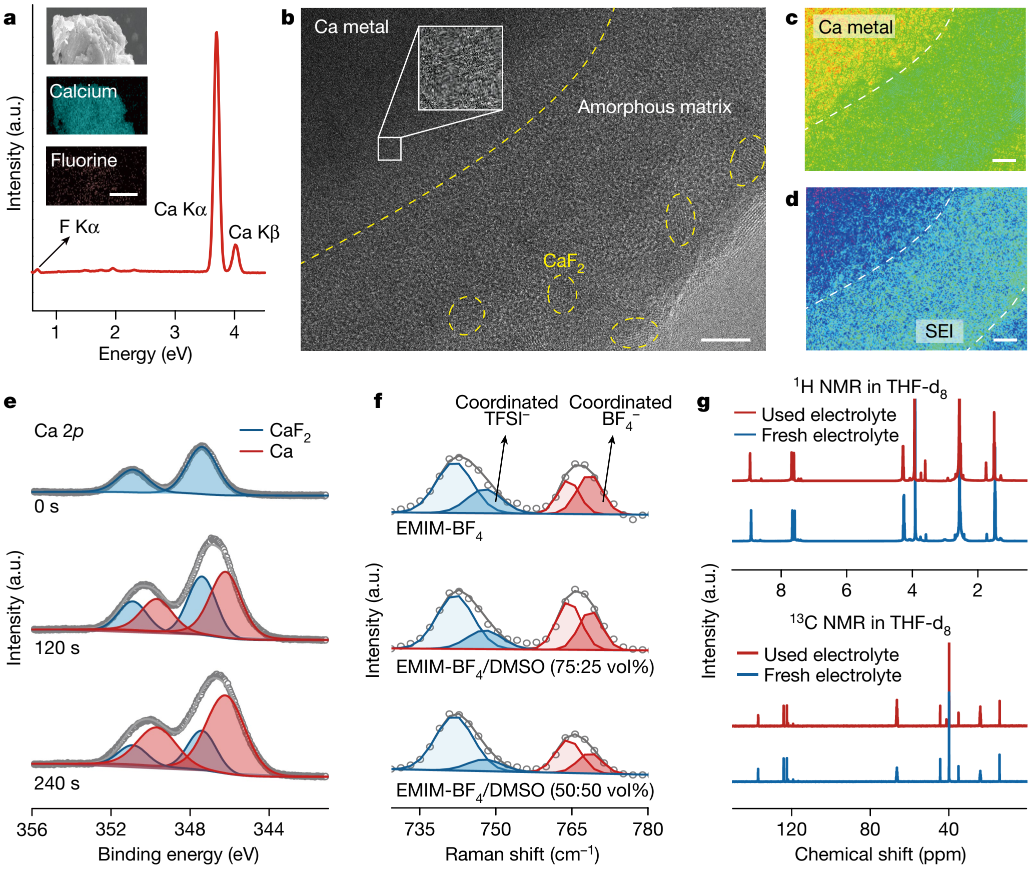

Fig. 3 | Optimized electrolyte facilitates stable operation of $Ca–O_2$ batteries. **a**, Energy-dispersive X-ray spectroscopy shows that the newly deposited Ca from the electrolyte contains Ca and a small proportion of F. Inset, elemental mapping of Ca deposits. **b**, CRYO-TEM image of Ca deposits obtained from the electrolyte. The dashed yellow line indicates the regions of Ca metal (left) and SEI (right). **c**, Distribution map of metallic Ca crystalline in **b** obtained by fast Fourier transformation (FFT) filtering using Ca (200) lattice spacing signal. The red region represents the metallic Ca-rich region as marked by the dashed white line. **d**, Distribution map of CaF_2 crystalline in **b** obtained by FFT filtering using CaF_2 (111) lattice spacing signal. The green region represents the CaF_2-rich region as marked by the dashed white line. **e**, Ca 2p XPS depth profiling spectra of Ca deposits show metallic Ca and CaF_2 (a component of SEI) are present. **f**, Raman spectra of electrolytes containing 0.5 M $Ca(TFSI)_2$ in different proportions of $EMIM-BF_4$ to DMSO. Coordination between Ca^{2+} and BF_4^-/$TFSI^-$ anions is relieved in the presence of DMSO. **g**, ^1H NMR (top) and ^{13}C NMR (bottom) spectra of fresh and used liquid electrolytes in tetrahydrofuran-d_8. THF, tetrahydrofuran; a.u., arbitrary units. Scale bars, 20 μm (**a**) and 5 nm (**b**–**d**).

the reversible Ca stripping–plating in $Ca–O_2$ batteries[28]. Cryogenic transmission electron microscopy (CRYO-TEM) images (Fig. 3b–d and Extended Data Fig. 4d) and X-ray photoelectron spectroscopy (XPS) depth profiling (Fig. 3e and Extended Data Fig. 4e) further confirmed that the recharged anode was composed of metallic Ca covered by a layer of CaF_2-rich SEI[22,28]. This SEI was found to be comprised of randomly dispersed small crystalline CaF_2 domains (diameters of about 3 nm) within surrounding amorphous organic compounds, including $–SO_xR$ (derived from DMSO and $TFSI^-$), $–CF_x$ (derived from $TFSI^-$) and a small proportion of $–CO_2–$ (Extended Data Table 1 and Extended Data Fig. 4f), which contribute to the Ca^{2+} conductivity and form the foundation for operation of $Ca–O_2$ batteries at room temperature.

We found that feasible battery reactions originate from our optimized electrolyte formulation, that is, the ionic liquid enables the oxidation stability (Extended Data Fig. 5) and DMSO co-solvent affords enhanced Ca^{2+}/O_2 transport (Extended Data Table 2 and Extended Data Fig. 6) with facilitated Ca plating–stripping (Extended Data Fig. 7). Importantly, compared with other electrolyte formulations that either contained less DMSO or no DMSO, our optimized electrolyte (0.5 M $Ca(TFSI)_2$ in 50:50 vol% DMSO:$EMIM-BF_4$) had the weakest $Ca^{2+}–BF_4^-$ (769 cm^{-1}) and $Ca^{2+}–TFSI^-$ (748 cm^{-1}) bands (Fig. 3f, Methods and Extended Data Fig. 8a–c), suggesting a reorganized Ca^{2+} coordination structure with reduced contact ion pairs[29,30]. This renders a decreased Ca^{2+} de-solvation energy barrier of 30.37 kJ mol^{-1} (Extended Data Fig. 8d–f) for facilitated Ca deposition and thus enhances anode reversibility, as evidenced by the improved cycling performance of Ca plating–stripping over 250 h in symmetric Ca||Ca cells[8] (Extended Data Fig. 8g). Furthermore, the nuclear magnetic resonance (NMR) spectra of fresh (as-prepared) and used (after 100 cycles at 0.1 mA cm^{-2} and 0.05 mAh cm^{-2}) electrolytes showed that the main components ($Ca(TFSI)_2$ and $EMIM-BF_4$) were intact on battery operation[16,31] (Fig. 3g; details in the Methods). Only a trace amount of dimethyl sulphone ($DMSO_2$, approximately 2.9 ppm) was observed after 100 cycles, which explained the slight deviation from the theoretical $e^-:O_2$ ratio of 2:1 in in situ DEMS measurements (Fig. 2a).

Benefited from the durable ionic liquid-based electrolyte, the $Ca–O_2$ batteries exhibited similar behaviours under either air or neat O_2 (Fig. 4a) and had a cycle life of 450 cycles in the air (at 1 A g^{-1} and 500 mAh g^{-1}; Extended Data Fig. 9a). We then extended the test of the $Ca–O_2$ battery in O_2 by determining its cycling response under various operation conditions. Under higher limited specific capacities of 1,000 mAh g^{-1} and 2,000 mAh g^{-1}, the cells showed no capacity fade with little increase in the voltage polarization after 270 and 150 cycles, respectively (Extended Data Fig. 9b). Similarly, the cells with an increased cathode loading (1.0 mg_{CNT} cm^{-2} at 0.5 mAh cm^{-2}) showed stable operation (Extended Data Fig. 9c). Furthermore, towards realistic application conditions, the $Ca–O_2$ batteries assembled with thin Ca anodes (5 mAh cm^{-2}) also achieved stable cycling for 240 h

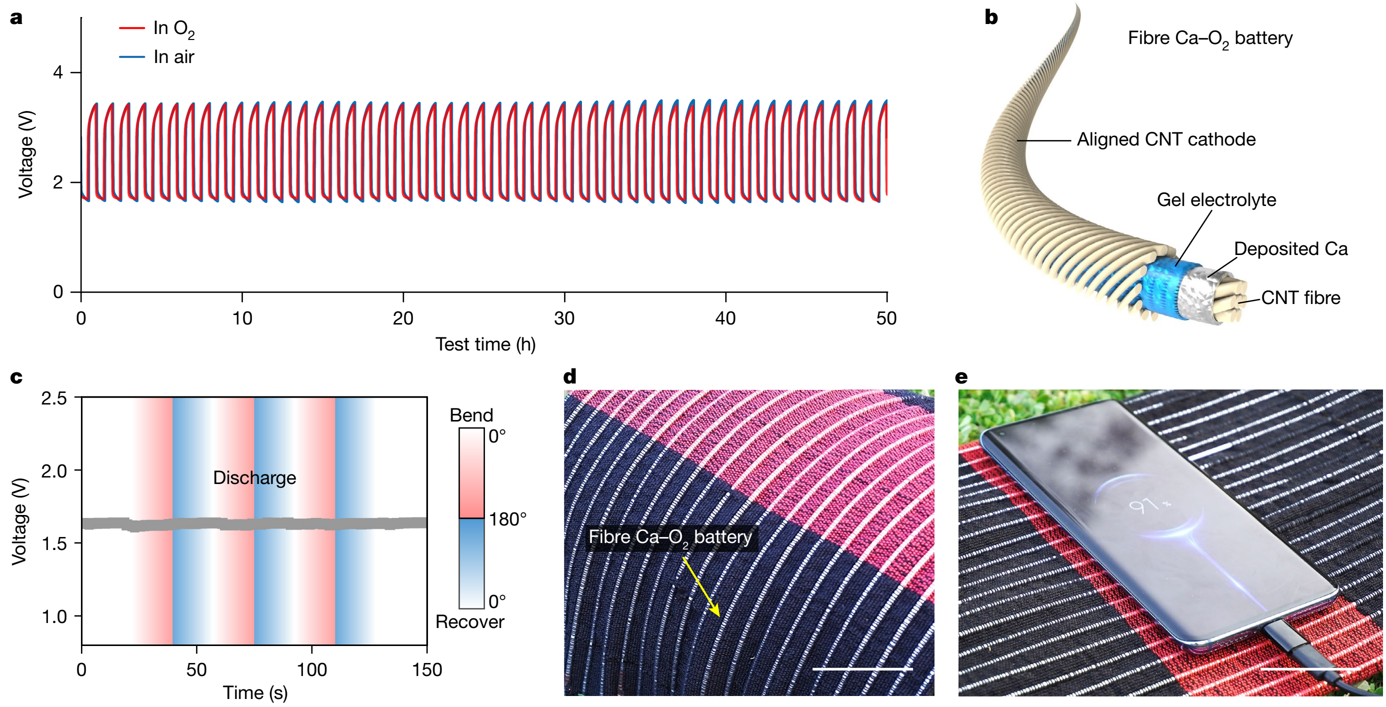

Fig. 4 | Ca–O_2 batteries are suitable for practical applications. a, Galvanostatic discharge–charge curves of the Ca–O_2 battery in the air (blue curve) and O_2 (red curve) overlap, indicating the battery is stable and durable in the air. **b**, Schematic of a fibre Ca–O_2 battery. Gel electrolyte is formed by adding a polymer composite of poly(vinylidene fluoride-*co*-hexafluoropropylene) and poly(trimethylolpropane ethoxylate triacrylate) to our optimized ionic liquid-based electrolyte and polymerized by ultraviolet irradiation for 10 s (see the Methods for details). **c**, Discharge curve of the fibre Ca–O_2 battery under dynamic bending and releasing shows a flat discharge plateau without intensive voltage fluctuation. **d**, Photograph of an energy-storage textile made from fibre Ca–O_2 batteries. **e**, Photograph of the battery textile charging a smartphone. Scale bar, 5 cm (**d** and **e**).

(60 cycles) under the conditions of a current density of 0.25 mA cm^{-2} and a capacity of 0.5 mAh cm^{-2} (Extended Data Fig. 9d,e). The gradually lowered discharge plateau was probably because of the consumption and passivation of active Ca in anodes. In this regard, we anticipate that Ca anodes could be further stabilized by electrolyte engineering, the development of artificial SEI and the fabrication of structured anodes, to afford enhanced cycling performance of Ca–O_2 batteries.

We sought to translate the Ca–O_2 batteries into wearable energy-storage solutions of safety and sustainability, because the electrochemical performance, low tendency of dendrite formation of Ca metal and the air-tolerant ionic liquid-based electrolyte well meet the requirements for wearable electronics. As a demonstration, we constructed a flexible Ca–O_2 fibre battery by coating a Ca-deposited CNT fibre anode with an ionic liquid-based gel electrolyte and then wrapping the fibre with an aligned CNT cathode sheet on the outside (Fig. 4b). Depositing Ca onto flexible CNT fibres could avoid the use of largely excessive Ca metal and the poor processability of monolithic Ca metal applied in conventional planar Ca batteries. When bent from 0° to 180°, the fibre battery continued to stably discharge with a plateau at about 1.7 V (Fig. 4c; details in Methods and Extended Data Fig. 10). Using a commercial braiding machine, we weaved these fibre batteries into breathable and flexible battery textiles (Fig. 4d) that can power electronic devices such as mobile phones (Fig. 4e).

In conclusion, we report a Ca–O_2 battery that can be reversibly operated at room temperature. We show that the dominant Ca–O_2 electrochemistry can rely on an efficient two-electron O_2 redox, instead of the sluggish four-electron process. This new understanding of cathode electrochemistry in Ca–O_2 batteries is expected to open avenues for designing and screening new cathode materials and electrolytes that can further unlock the full theoretical capacity of Ca metal. Our Ca–O_2 battery demonstrates cycling stability and can be made into flexible fibres for textile batteries. We believe our results will turn the cost-effective Ca chemistry into a promising, sustainable energy-storage technology.

Online content

Any methods, additional references, Nature Portfolio reporting summaries, source data, extended data, supplementary information, acknowledgements, peer review information; details of author contributions and competing interests; and statements of data and code availability are available at https://doi.org/10.1038/s41586-023-06949-x.

1. Liang, Y., Dong, H., Aurbach, D. & Yao, Y. Current status and future directions of multivalent metal-ion batteries. *Nat. Energy* **5**, 646–656 (2020).
2. Hou, S. et al. Solvation sheath reorganization enables divalent metal batteries with fast interfacial charge transfer kinetics. *Science* **374**, 172–178 (2021).
3. Li, M. et al. Design strategies for nonaqueous multivalent-ion and monovalent-ion battery anodes. *Nat. Rev. Mater.* **5**, 276–294 (2020).
4. Arroyo-de Dompablo, M. E., Ponrouch, A., Johansson, P. & Palacín, M. R. Achievements, challenges, and prospects of calcium batteries. *Chem. Rev.* **120**, 6331–6357 (2020).
5. Song, H. & Wang, C. Current status and challenges of calcium metal batteries. *Adv. Energy Sustain. Res.* **3**, 2100192 (2022).
6. Wang, D. et al. Plating and stripping calcium in an organic electrolyte. *Nat. Mater.* **17**, 16–20 (2018).
7. Dong, H. et al. High-power Mg batteries enabled by heterogeneous enolization redox chemistry and weakly coordinating electrolytes. *Nat. Energy* **5**, 1043–1050 (2020).
8. Sun, W. et al. A rechargeable zinc-air battery based on zinc peroxide chemistry. *Science* **371**, 46–51 (2021).
9. Ponrouch, A., Frontera, C., Bardé, F. & Palacín, M. R. Towards a calcium-based rechargeable battery. *Nat. Mater.* **15**, 169–172 (2016).
10. Lu, Y., Neale, A. R., Hu, C. & Hardwick, L. J. Divalent nonaqueous metal-air batteries. *Front. Energy Res.* **8**, 602918 (2021).
11. Wang, M. et al. Reversible calcium alloying enables a practical room-temperature rechargeable calcium-ion battery with a high discharge voltage. *Nat. Chem.* **10**, 667–672 (2018).
12. Forero-Saboya, J. et al. Understanding the nature of the passivation layer enabling reversible calcium plating. *Energy Environ. Sci.* **13**, 3423–3431 (2020).
13. Zhao-Karger, Z. et al. Calcium-tin alloys as anodes for rechargeable non-aqueous calcium-ion batteries at room temperature. *Nat. Commun.* **13**, 3849 (2022).

14. Jie, Y. et al. Electrolyte solvation manipulation enables unprecedented room-temperature calcium-metal batteries. *Angew. Chem. Int. Ed.* **59**, 12689–12693 (2020).
15. Gao, X. et al. Alkoxy-functionalized ionic liquid electrolytes: understanding ionic coordination of calcium ion speciation for the rational design of calcium electrolytes. *Energy Environ. Sci.* **13**, 2559–2569 (2020).
16. Asadi, M. et al. A lithium-oxygen battery with a long cycle life in an air-like atmosphere. *Nature* **555**, 502–506 (2018).
17. Aurbach, D., McCloskey, B. D., Nazar, L. F. & Bruce, P. G. Advances in understanding mechanisms underpinning lithium–air batteries. *Nat. Energy* **1**, 16128 (2016).
18. Chi, X. et al. A highly stable and flexible zeolite electrolyte solid-state Li-air battery. *Nature* **592**, 551–557 (2021).
19. Pujare, N. U., Semkow, K. W. & Sammells, A. F. A calcium oxygen secondary battery. *J. Electrochem. Soc.* **135**, 260–261 (1988).
20. Shiga, T., Kato, Y. & Hase, Y. Coupling of nitroxyl radical as an electrochemical charging catalyst and ionic liquid for calcium plating/stripping toward a rechargeable calcium-oxygen battery. *J. Mater. Chem. A* **5**, 13212–13219 (2017).
21. Li, T., Zhang, X,-Q., Shi, P. & Zhang, Q. Fluorinated solid-electrolyte interphase in high-voltage lithium metal batteries. *Joule* **3**, 2647–2661 (2019).
22. Li, Z., Fuhr, O., Fichtner, M. & Zhao-Karger, Z. Towards stable and efficient electrolytes for room-temperature rechargeable calcium batteries. *Energy Environ. Sci.* **12**, 3496–3501 (2019).
23. Lai, J. et al. Electrolytes for rechargeable lithium–air batteries. *Angew. Chem. Int. Ed.* **59**, 2974–2997 (2020).
24. Ye, L. et al. Stabilizing lithium into cross-stacked nanotube sheets with an ultra-high specific capacity for lithium oxygen batteries. *Angew. Chem. Int. Ed.* **58**, 2437–2442 (2019).
25. Nishioka, K. et al. Isotopic depth profiling of discharge products identifies reactive interfaces in an aprotic Li–O_2 battery with a redox mediator. *J. Am. Chem. Soc.* **143**, 7394–7401 (2021).
26. Jung, H. et al. An improved high-performance lithium–air battery. *Nat. Chem.* **4**, 579–585 (2012).
27. Kondori, A. et al. A room temperature rechargeable Li_2O-based lithium-air battery enabled by a solid electrolyte. *Science* **379**, 499–505 (2023).
28. Shyamsunder, A., Blanc, L. E., Assoud, A. & Nazar, L. F. Reversible calcium plating and stripping at room temperature using a borate salt. *ACS Energy Lett.* **4**, 2271–2276 (2019).
29. Ko, S., Yamada, Y. & Yamada, A. An overlooked issue for high-voltage Li-ion batteries: suppressing the intercalation of anions into conductive carbon. *Joule* **5**, 998–1009 (2021).
30. Yu, Y. et al. A renaissance of *N*,*N*-dimethylacetamide-based electrolytes to promote the cycling stability of Li–O_2 batteries. *Energy & Environ. Sci.* **13**, 3075–3081 (2020).
31. Feng, S. et al. Molecular design of stable sulfamide- and sulfonamide-based electrolytes for aprotic Li-O_2 batteries. *Chem* **5**, 2630–2641 (2019).

Methods

Preparation of aligned CNT cathode

Aligned CNT cathodes were prepared by stacking aligned CNT sheets drawn from a spinnable CNT array. Spinnable CNT arrays were synthesized by a chemical vapour deposition method. Aluminium oxide (3 nm) and iron (1.2 nm) were deposited in order on a silicon wafer as catalysts. Ethylene (90 sccm), argon (400 sccm) and hydrogen (30 sccm) were used as the carbon source, carrier gas and reducing gas for chemical vapour deposition, respectively. The spinnable CNT array with a thickness of around 200 μm was synthesized at a temperature of 750 °C in a tube furnace. Freestanding aligned CNT films were drawn from the spinnable CNT array by a blade. CNT air cathodes (0.1–5 mg cm^{-2}) were fabricated by stacking above aligned CNT layers and could be directly used for cell assembly without additional binders and conductive agents.

Fabrication of Ca–O_2 batteries

The battery cell was assembled in an air-tight Swagelok cell (for details of battery mould, refer to http://linglush.com/en/) using commercial pure Ca chips (>99.5%, thickness of 500 μm; Baotou Jinghua Calcium Metal Industry) as the anode and freestanding aligned CNT film (0.1 mg cm^{-2}) as the cathode. The practical working area was 1 cm^2 for both aligned CNT air cathode and metallic Ca anode. All metallic Ca anodes were polished to remove possible passivation layers before use. The weight of the aligned CNT cathode was measured by a Sartorious ultra-micro balance (MCA 2.7 S 2CCN F QP99) with a scale interval of 0.1 μg. A glass fibre separator (16 mm in diameter) was used for cell assembly. The electrolyte (water content <50 ppm) was composed of 0.5 M calcium bis(trifluoromethanesulphonimide) ($\mathrm{Ca(TFSI)_2}$, >99.5%) in 1-ethyl-3-methylimidazolium tetrafluoroborate (EMIM-$\mathrm{BF_4}$, >99.8%) and anhydrous dimethyl sulphoxide (DMSO, >99.9%) with a volume ratio of 50:50 vol%. Freshly activated 4 Å molecular sieves were added to remove residual water in the electrolyte for 48 h before use and the usage of electrolyte was 50 μl for each cell. The cell was assembled in a glovebox filled with ultrahigh purity argon (H_2O < 0.1 ppm, O_2 < 0.1 ppm). The Ca–O_2 battery was first purged with pure O_2 for 30 min and then sealed under 1 atm O_2 for electrochemical characterizations.

Electrochemical measurements

For discharge–charge experiments, the Ca–O_2 Swagelok battery setup consisting of aligned CNT film (working area of 1 cm^2, 0.1 mg) as the cathode, 0.5 M $\mathrm{Ca(TFSI)_2}$ as the Ca salt in EMIM-$\mathrm{BF_4}$/DMSO (50:50 vol%) as the electrolyte and metallic Ca chip (working area of 1 cm^2, thickness of 500 μm) as the anode was operated under a specific capacity-controlled mode with a constant applied current density on an Arbin electrochemical station (MSTATS-5V/10 mA/16Ch). The specific capacity and applied current density were calculated by the weight of aligned CNT cathode. Linear sweep voltammetry experiments were performed on a CHI 660D electrochemical workstation. For anodic linear sweep voltammetry experiments of ionic liquid-based electrolytes, the coin cell consisting of Ca chip (as the counter and reference electrodes) and CNT working electrode was operated with a scan rate of 1 mV s^{-1} from 1.5–6 V (compared with Ca/Ca^{2+}). For electrochemical impedance spectroscopy tests, the symmetric coin cell consisting of two Ca chips was operated on a CHI 660D electrochemical workstation with a frequency range from 10^{-2} Hz to 10^5 Hz and an amplitude of 5 mV.

Characterization techniques

Scanning electron microscopy and energy-dispersive X-ray spectroscopy measurements were carried out on Gemini 500 scanning electron microscopy. Transmission electron microscopy measurements were performed on JEOL JEM-2100F operated at 200 kV. Cryo-transmission electron microscopy measurements were performed under liquid nitrogen temperature on JEM-Z300FSC (CRYO ARM 300) operated at 300 kV equipped with a Gatan K3 direct electron detector. The images were recorded in a close-to-focus condition with an electron dose of 100 e^- $Å^{-2}$. The distribution maps of crystalline materials were obtained by applying masks to corresponding lattice spacing signals in the FFT of the images. The masked areas were kept and then used for inverse FFT, and the resultant maps were coloured based on the pixel intensities. X-ray diffraction analysis was conducted on an X-ray powder diffractometer (Bruker AXSD8) with filtered Cu Kα radiation. Raman analysis was conducted on Horiba Jobin Yvon XploRA. Raman spectra of ionic liquid-based electrolytes were obtained using a laser (638 nm) with 2 cm^{-1} resolution. The proportion of Ca^{2+}-coordinated $\mathrm{BF_4}^-$/TFSI^- was obtained by normalizing the integrated scattering intensity of the band for coordinated $\mathrm{BF_4}^-$/TFSI^- to the total peak areas. X-ray photoelectron spectroscopy experiments were performed on a Thermo Scientific K-Alpha scanning XPS microscope operated at 15 kV and 15 mA. NMR measurements of the electrolyte composition were conducted on a Bruker AVANCE III HD 500 instrument. Fifty microlitres of electrolyte was extracted from the cycled cells and then diluted with 0.6 ml of THF-d_8. A calcium-chloride-saturated deuterium water was used to obtain the reference chemical shift of $^{43}\mathrm{Ca}$. TOF-SIMS measurement was taken using TOF-SIMS 5–100 (ION-TOF) with Bi^{3+} primary beam (30 keV with 100 × 100 $\mu\mathrm{m}^2$ spot size) and Cs^+ secondary gun (2 keV with 300 × 300 $\mu\mathrm{m}^2$ analysis area). The apparent viscosity of electrolytes was measured by a Thermofisher HAAKE MARS III rotational rheometer at room temperature. The ionic conductivity of electrolytes was measured by a Leici DDS-307A ionic conductor at room temperature. The specific surface area of the aligned CNT cathode composite was measured by an automatic specific surface area and porosity analyser (Quadrasorb evo). Noting that for post-cycling characterization, the cells were dissembled in a glovebox, and the electrodes were rinsed with anhydrous DMSO and dried under vacuum before further characterization.

The differential DEMS experiment was carried out in a custom-made battery (http://linglush.com/en/) with two poly(ether-ether-ketone) capillary tubes for gas inlet and outlet. The experimental setup consisted of a LAND battery testing system (CT2001A, Wuhan LAND Electronic) and a quadrupole mass spectrometry (Hiden HPR-40 DEMS). The DEMS was calibrated by injecting into the mass spectrometer standard samples of pure O_2 (>99.99%) in research-grade argon (>99.99%) at known concentrations and measuring the corresponding partial pressures of O_2. The cathode loading was 1 mg cm^{-2} and the charging–discharging rate was 1 mA cm^{-2} to enhance the O_2 mass spectrometry signal.

The Ca^{2+} transference number ($t_{\mathrm{Ca}^{2+}}$) of ionic liquid-based electrolytes was measured using the Bruce–Vincent method. Potentiostatic polarization measurements were conducted with an applied potential of 10 mV in the symmetric coin cell consisting of two Ca chips until the current reached a steady state, and corresponding electrochemical impedance spectroscopy data were collected before and after the potentiostatic polarization. The $t_{\mathrm{Ca}^{2+}}$ was calculated according to:

$$t_{\mathrm{Ca}^{2+}} = \frac{I_{\mathrm{ss}}(\Delta V - I_0 R_0)}{I_0(\Delta V - I_{\mathrm{ss}} R_{\mathrm{ss}})}$$

where ΔV is the applied potential, I_0 is the initial current, R_0 is the initial resistance, I_{ss} is the steady-state current and R_{ss} is the steady-state resistance.

Rotating disc electrode measurements were carried out in a three-electrode cell consisting of a glassy carbon electrode (5 mm in diameter, as the working electrode) and two Ca chips (1 cm^2, as the counter and reference electrodes). The experimental setup consisted of an Autolab electrochemical workstation (Metrohm Autolab M204) and a PINE AFMSRCE rotator. The data were collected in the voltage range of 1.0–2.0 V compared with Ca/Ca^{2+} at a scan rate of 100 mV s^{-1}. The rotation rates were at 400, 600, 800, 1,000 and 1,200 rpm. The diffusion coefficient (D) was calculated according to the Levich equation:

$$i_{\mathrm{Lim}} = 0.62nFD^{2/3}\omega^{1/2}\upsilon^{-1/6}C$$

where i_{Lim} is the limiting current density, n is the number of electrons transferred ($n = 2$ for two electrons), F is Faraday's constant (96,485 C mol^{-1}), C is the concentration of redox species (2.15 mM for 0.5 M $Ca(TFSI)_2$ in EMIM-BF_4/DMSO (50:50 vol%), 2.98 mM for 0.5 M $Ca(TFSI)_2$ in EMIM-BF_4), ω is the routing angular rotation rate (rad/s) and v is the kinetic viscosity (0.1392 cm^2 s^{-1} for 0.5 M $Ca(TFSI)_2$ in EMIM-BF_4:DMSO (50:50 vol%), 0.4788 cm^2 s^{-1} for 0.5 M $Ca(TFSI)_2$ in EMIM-BF_4).

The quantification measurement of CaO_2 was carried out through a peroxide titration technique based on the following equations:

$$CaO_2 + 2H_2O \rightarrow Ca(OH)_2 + H_2O_2$$

$$H_2O_2 + TiOSO_4 \rightarrow TiO_2SO_4 + H_2O$$

The CaO_2 was first hydrolysed to form calcium hydroxide ($Ca(OH)_2$) and hydrogen peroxide (H_2O_2). The titanium oxysulphate ($TiOSO_4$) was then oxidized by H_2O_2 to generate the yellow-coloured $[Ti(O_2)]^{2+}$ complex for the UV–vis detection. The standard curve was established by recording the UV–vis spectrum of a mixed solution of H_2O_2 (1 ml, 0–2 mM in water) and $TiOSO_4$ (1 ml, 15 wt% in dilute sulphuric acid). The precise concentration of the H_2O_2 standard solution was determined by potassium permanganate titration. The cathodic solution was prepared by transferring the discharged CNT cathode into 4 ml water. Similar to the standard solution, the cathodic solution (1 ml) and $TiOSO_4$ solution (1 ml) were introduced in a quartz cuvette for UV–vis spectroscopic analysis.

The activation energy of Ca^{2+} de-solvation in the ionic liquid-based electrolyte was measured using a temperature-dependent electrochemical impedance spectroscopy test in a symmetric coin cell consisting of two Ca chips. The cells were first cycled at 0.2 mA cm^{-2} and 0.2 mAh cm^{-2} for 10 cycles to form SEI on the Ca metal surface. Then the electrochemical impedance spectroscopy tests were carried out under temperatures at 30 °C, 40 °C, 50 °C and 60 °C. The activation energy could be evaluated according to the classic Arrhenius law:

$$\frac{1}{R_{\mathrm{CT}}} = A_0 e^{-E_a/RT}$$

where R_{CT} is the charge transfer resistance, A_0 is the pre-exponential constant, R is the standard gas constant, E_a is the activation energy and T is the absolute temperature. The activation energy was derived from the slope of $\ln(1/R_{\mathrm{CT}})$ compared with reciprocal temperature $1{,}000/T$ plot:

$$E_a = -8.314 \times \text{slope (kJ mol}^{-1}\text{)}$$

Density functional theory calculations

Density functional theory calculations were performed using the Perdew–Burke–Ernzerhof[32] exchange-correlation functional as implemented in the Vienna Ab-Initio Simulation Package[33]. The valence electronic states were expanded based on plane waves with the core–valence interaction represented using the Projector Augmented Plane Wave approach[34] and a kinetic energy cutoff of 520 eV. The Brillouin zone integration was sampled with 2 × 2 × 1 K-point meshes for the optimization of geometry. The convergence threshold was set to 10^{-5} eV in energy and 0.02 eV $Å^{-1}$ in force. A vacuum layer of 18 Å was applied for all calculated models. A 5 × 5 zig-zag monolayer graphene was used as the fundamental model to manifest the structure of the cathode. A 5 × 5 supercell was used to eliminate the interaction of adsorbed species and their images.

The O_2 reduction processes were calculated using the following equations. During discharging, the first step is the adsorption of O_2 on the CNT cathode surface to form O_2^* (*, active site):

$$O_2 + {}^* \rightarrow O_2^* \tag{1}$$

Then O_2^* is electrochemically reduced and combined with Ca^{2+} to form the OOCa* intermediate by a two-electron transfer process:

$$O_2^* + Ca^{2+} + 2e^- \rightarrow OOCa^* \tag{2}$$

OOCa* can be further combined with another adsorbed O_2 to form the CaO_4^* intermediate:

$$OOCa^* + O_2^* \rightarrow CaO_4^* \tag{3}$$

which is further electrochemically reduced and combined with Ca^{2+} to form the CaO_2 discharge product:

$$CaO_4^* + Ca^{2+} + 2e^- \rightarrow 2CaO_2 \tag{4}$$

This completes the two-electron pathway per O_2. By contrast, for the four-electron reaction pathway (per O_2), the OOCa* intermediate is electrochemically reduced directly and combined with another Ca^{2+} to form the $Ca_2O_2^*$ intermediate. The latter is eventually converted to the CaO discharge product:

$$OOCa^* + Ca^{2+} + 2e^- \rightarrow Ca_2O_2^* \tag{5}$$

$$Ca_2O_2^* \rightarrow 2CaO \tag{6}$$

During battery recharging, the decomposition of CaO_2 occurs through a reversed process of the above-mentioned reactions, in which Ca^{2+} and O_2 are dissociated from CaO_2 driven by a charging potential.

The free energies of the adsorbed clusters were calculated using the total energies of the solid-state compounds and the free energy of the gas phase O_2:

$$\Delta G_{\mathrm{ad}} = G_{\mathrm{substrate+molecule}} - G_{\mathrm{substrate}} - G_{\mathrm{molecule}}$$

where $G_{\mathrm{substrate+molecule}}$, $G_{\mathrm{substrate}}$ and G_{molecule} are the energies of the whole system, the substrate and the gas phase molecule, respectively.

Fabrication of flexible-fibre Ca–O_2 batteries

Fibre Ca–O_2 battery was fabricated in a co-axial configuration and composed of a metallic Ca-coated CNT fibre as the anode, a layer of continuous, aligned CNT film as the air cathode and a gel electrolyte layer between the inner anode fibre and the outer air cathode layer. For the fibre anode, metallic Ca was electrodeposited onto an aligned CNT fibre (synthesized using a floating-catalyst chemical vapour deposition method[35]) through a potentiostatic electrodeposition method (potential set at −0.5 V compared with Ca/Ca^{2+} for 40 min) in electrolyte comprising of 0.5 M $Ca(TFSI)_2$ in EMIM-BF_4:DMSO (50:50 vol%) with a Ca chip as both counter and reference electrodes. The Ca loading mass was 0.5 ± 0.05 mg cm^{-1} for the fibre anode. The fibre anode was then dip-coated with a thin layer of gel electrolyte comprising of the same electrolyte formulation applied in the Ca–O_2 Swagelok cell and an additional polymeric framework. The gel electrolyte was prepared by mixing three types of solution, that is, 0.5 M $Ca(TFSI)_2$ in EMIM-BF_4:DMSO (50:50 vol%), 1.168 g poly(vinylidene fluoride-*co*-hexafluoropropylene) dissolved in 4.672 g *N*-methyl-2-pyrrolidinone and 0.012 g 2-hydroxy-2-methyl-1-phenyl-1-propanone dissolved in 3.504 g trimethylolpropane ethoxylate triacrylate, at ratios of 33:42:25 wt%. Then the above mixed, precursor solution was uniformly coated onto the fibre anode followed by an ultraviolet irradiation (365 nm) treatment of 10 s to form the gel electrolyte layer acting as both electrolyte and separator in fibre batteries. A continuous layer of the aligned CNT strips was wrapped onto the gel electrolyte-coated fibre with a loading mass of 0.05 ± 0.01 mg cm^{-1} as the air cathode. Stainless steel lead wires were connected with electrode layers inside the fibre batteries for electrochemical tests. A custom-made extruder described previously[36] was used to encapsulate the fibre battery into a low-density polyethylene tube (diameter of 1 mm) of highly selective O_2 penetration. The encapsulated fibre battery was flexible and could withstand bending (bending radius of 4 mm) for operations. Fibre batteries were woven into textile on a rapier loom (Tong Yuan Textile Machinery)[37].

Data availability

The data that support the findings of this study are available from the corresponding authors upon request. Source data are provided with this paper.

32. Perdew, J. P., Burke, K. & Ernzerhof, M. Generalized gradient approximation made simple. *Phys. Rev. Lett.* **77**, 3865–3868 (1998).
33. Kresse, G. & Furthmuller, J. Efficient iterative schemes for *ab initio* total-energy calculations using a plane-wave basis set. *Phys. Rev. B* **54**, 11169–11186 (1996).
34. Blöchl, P. E. Projector augmented-wave method. *Phys. Rev. B* **50**, 17953–17979 (1994).
35. Liu, Q. et al. Interlocked CNT networks with high damping and storage modulus. *Carbon* **86**, 46–53 (2015).
36. He, J. et al. Scalable production of high-performing woven lithium-ion fibre batteries. *Nature* **597**, 57–63 (2021).
37. Liao, M. et al. Industrial scale production of fibre batteries by a solution-extrusion method. *Nat. Nanotechnol.* **17**, 372–377 (2022).

Acknowledgements This work was supported by MOST (2022YFA1203002, 2022YFA1203001), NSFC (T2321003, 22335003, 52122310, 22075050, 52222310, T2222005, 22175042, 22225201) and STCSM (21511104900, 20JC1414902). We thank A.-L. Chun of Science Storylab for reading and editing the paper.

Author contributions H.P., Y. Wang, H.Z., J.L. and B.W. conceived and designed the research project. L.Y., M.L. and K.Z. performed the experiments on Ca–O_2 batteries, fibre batteries and the simulations of reaction pathways. M.Z., Y.J., X.C., C.T., P.L. and Y. Wen performed electrochemical measurements of Ca–O_2 batteries. C.W. performed experiments on the textile batteries. Q.X. collected the TOF-SIMS characterization data. Y. Xu collected the cryo-TEM characterization data. X.S., P.C., H.S., Y.G., Y.Z., Y. Xia and X.X. analysed the data. All the authors discussed the data and wrote the paper.

Competing interests The authors declare no competing interests.

Additional information
Supplementary information The online version contains supplementary material available at https://doi.org/10.1038/s41586-023-06949-x.
Correspondence and requests for materials should be addressed to Bingjie Wang, Jun Lu, Haoshen Zhou, Yonggang Wang or Huisheng Peng.
Peer review information *Nature* thanks the anonymous reviewers for their contribution to the peer review of this work.

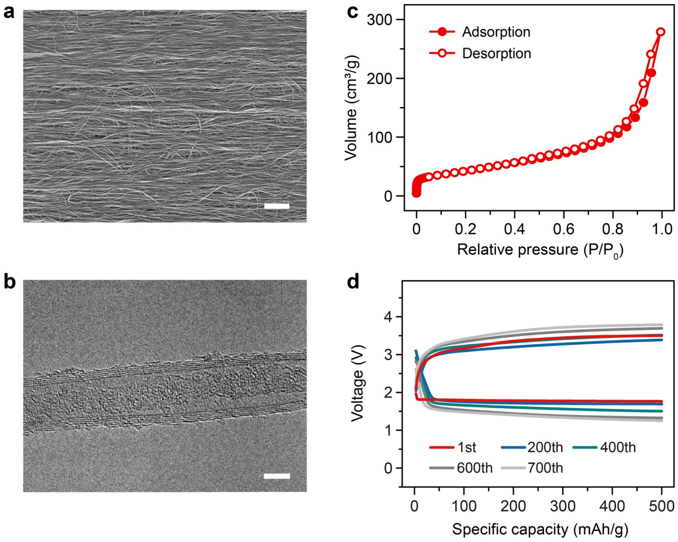

Extended Data Fig. 1 | Characterization of CNT air cathode and cycling performance of the Ca-O_2 battery. a, **b**, SEM (**a**) and TEM (**b**) images of CNT cathode. Scale bars, 1 µm (**a**), 5 nm (**b**). **c**, Nitrogen adsorption-desorption isotherm of the CNT, indicating a specific surface area of 172.5 m^2/g. **d**, Galvanostatic discharge and charge curves of Ca-O_2 battery at a current density of 1 A/g and a specific capacity of 500 mAh/g for 700 cycles.

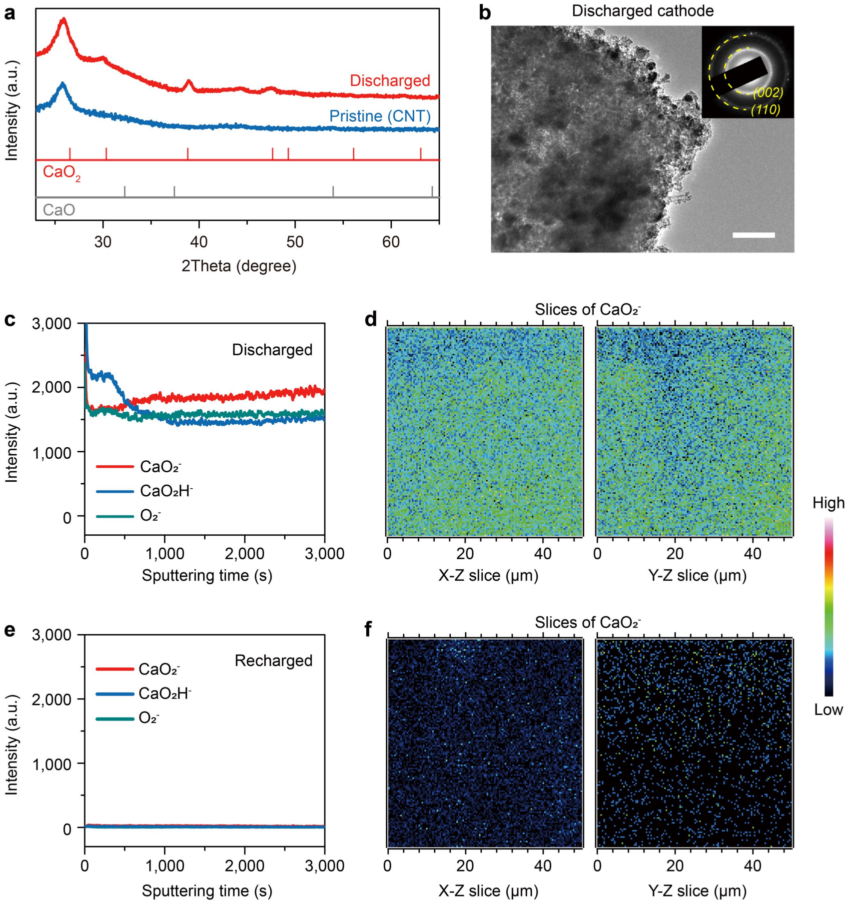

Extended Data Fig. 2 | Characterization of the discharge product in Ca-O_2 batteries. **a**, XRD patterns of the cathode after the 1st discharge and the pristine cathode (CNT) suggesting that the main discharge product of Ca-O_2 batteries at room temperature is CaO_2. References: CaO_2 (mp-634859) and CaO (mp-2605) from the Materials Project database. **b**, TEM image and the corresponding selected area electron diffraction (SAED) pattern (inset) of the discharge product. Scale bar, 100 nm. **c**, Tof-SIMS depth profile of various secondary ion species obtained by sputtering the fully discharged cathode, indicating the formation of CaO_2 in the discharge process. **d**, Tof-SIMS two-dimensional view images of CaO_2^- from the discharged cathode showing the uniform distribution of CaO_2. **e**, Tof-SIMS depth profile of various secondary ion species obtained by sputtering the recharged cathode, indicating the decomposition of CaO_2 in the charge process. **f**, Tof-SIMS two-dimensional view images of CaO_2^- from the recharged cathode showing the decomposition of CaO_2.

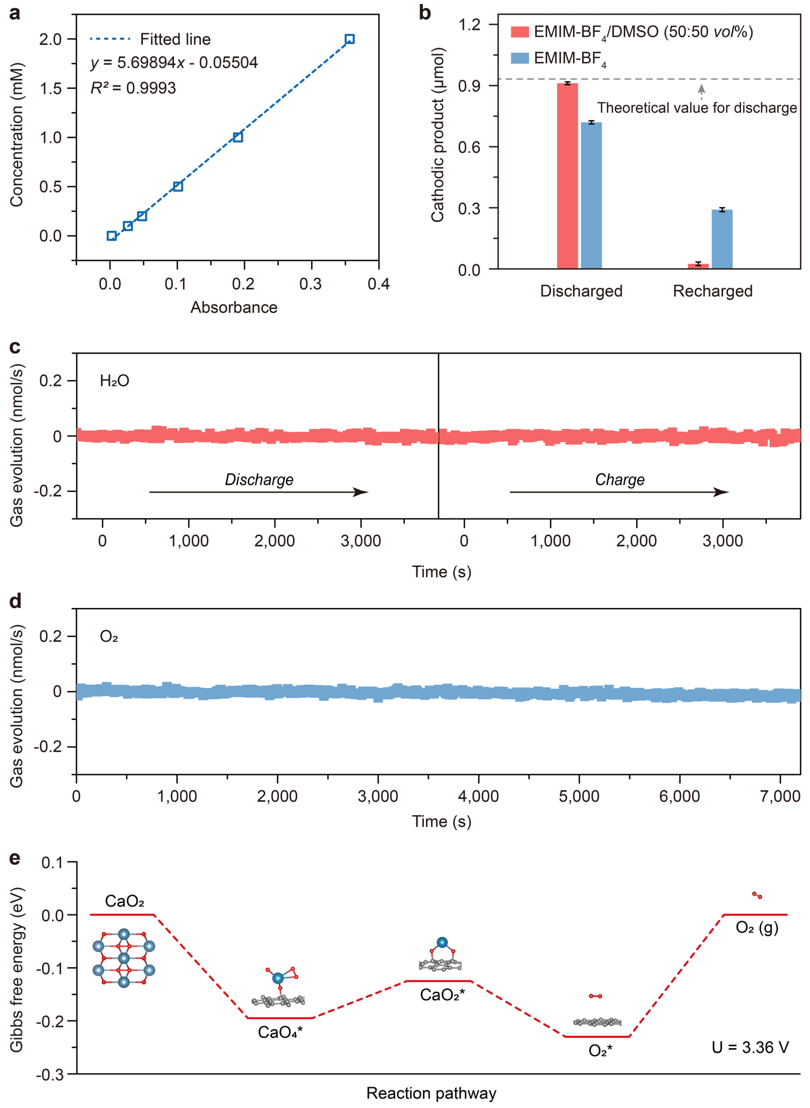

Extended Data Fig. 3 | Reversibility of CaO_2 formation/decomposition in Ca-O_2 cell chemistry. a, The standard curve of the $[Ti(O_2)]^{2+}$ complex concentration obtained from the UV-*vis* spectrometer for the quantitative titration measurement of CaO_2. **b**, The amount of cathodic products upon discharge/recharge derived from the titration measurements, using the optimized electrolyte (EMIM-BF_4/DMSO, 50:50 *vol*%, red bars) and the contrast electrolyte (EMIM-BF_4 without DMSO, blue bars). The results show that, in the optimized electrolyte (EMIM-BF_4/DMSO, 50:50 *vol*%), 97.3% of the CaO_2 discharge product can be decomposed upon recharge, pointing to a higher reversibility (97.3%) than that of the contrast electrolyte (<60%). Error bars represent the standard deviations of the results from five samples. **c**, DEMS profiles showing that the H_2O signal during discharging and charging keep below 0.05 nmol/s, indicating the absence of the potential parasitic reaction between CaO_2 and hydrofluoric acid (HF). **d**, DEMS profile at open circuit voltage showing the absence of O_2 evolution (<0.05 nmol/s) from the potential CaO_2 decomposition. **e**, Calculated Gibbs free energy of O_2 release from CaO_2 on the aligned CNT cathode, suggesting the feasibility of CaO_2 decomposition during the charge process in Ca-O_2 batteries. Note that an applied potential (U = 3.36 V *versus* Ca/Ca^{2+}) is used in order to simulate the charging process, which, in turn, leads to different Gibbs free energy values for the intermediates CaO_4* with respect to CaO_2 here, as compared to those in the discharge process (Fig. 2d).

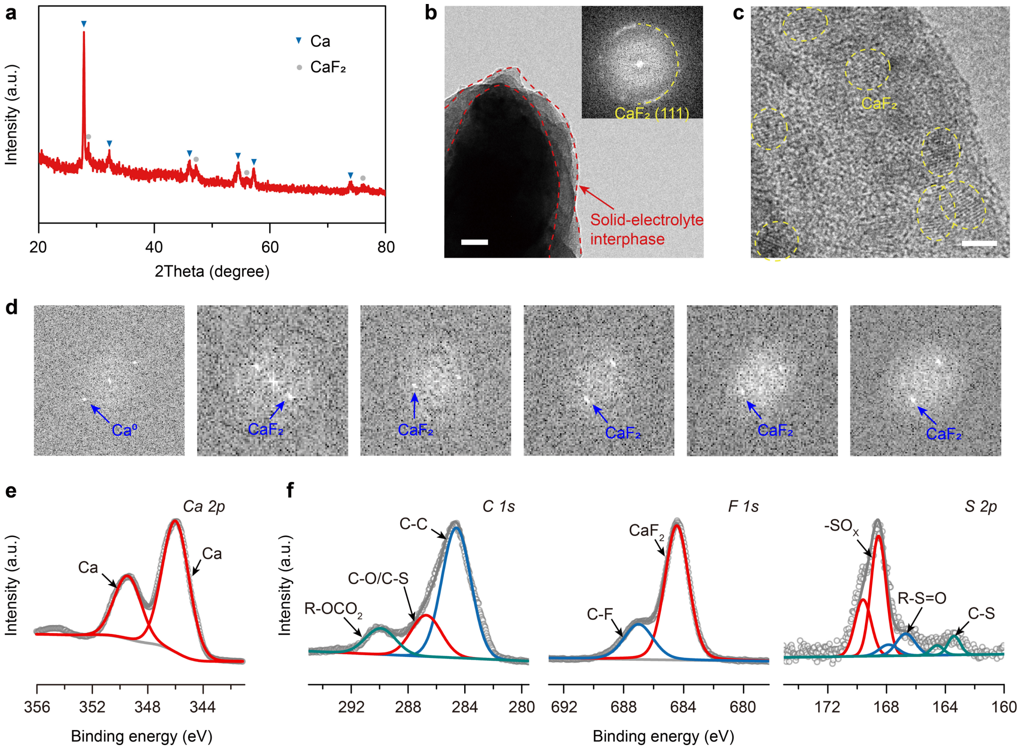

Extended Data Fig. 4 | Characterization of Ca metal anode disassembled from Ca-O_2 batteries. a, XRD pattern of the Ca anode disassembled from a charged Ca-O_2 battery showing the presence of metallic Ca and CaF_2. **b**, **c**, TEM images and the corresponding SAED pattern (inset) of the cycled Ca metal anode. Scale bars, 20 nm (**b**), 3 nm (**c**). **d**, Fast Fourier transform (FFT) images of the crystal regions marked in Fig. 3b showing the presence of metallic Ca (cubic Fm3m crystal phase, (200) plane) and randomly dispersed CaF_2 nanocrystals (cubic Fm3m crystal phase, (111) plane). **e**, XPS Ca 2p spectrum (after etching) of pure Ca metal displaying two peaks centered at 349.5 (Ca $2p_{1/2}$) and 346.0 eV (Ca $2p_{3/2}$). **f**, XPS C 1 s, F 1 s, and S 2p spectra of the cycled Ca metal anode, revealing a hybrid SEI composed of inorganic CaF_2 and organic compounds.

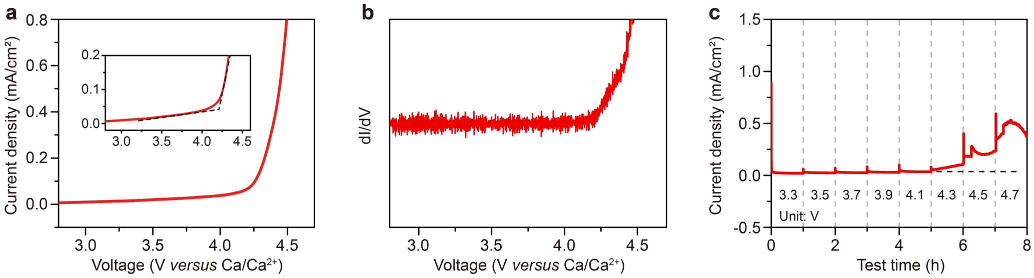

Extended Data Fig. 5 | Evaluation of oxidation stability of the electrolyte. **a**, Linear sweep voltammetry curves of our ionic liquid-based electrolyte on CNT electrode at a scan rate of 1.0 mV/s. Inset, the zoomed-in plot. **b**, The corresponding current derivative from **a**. **c**, Potentiostatic polarization of the Ca||CNT cell, suggesting an oxidation voltage over 4.1 V for our ionic liquid-based electrolyte.

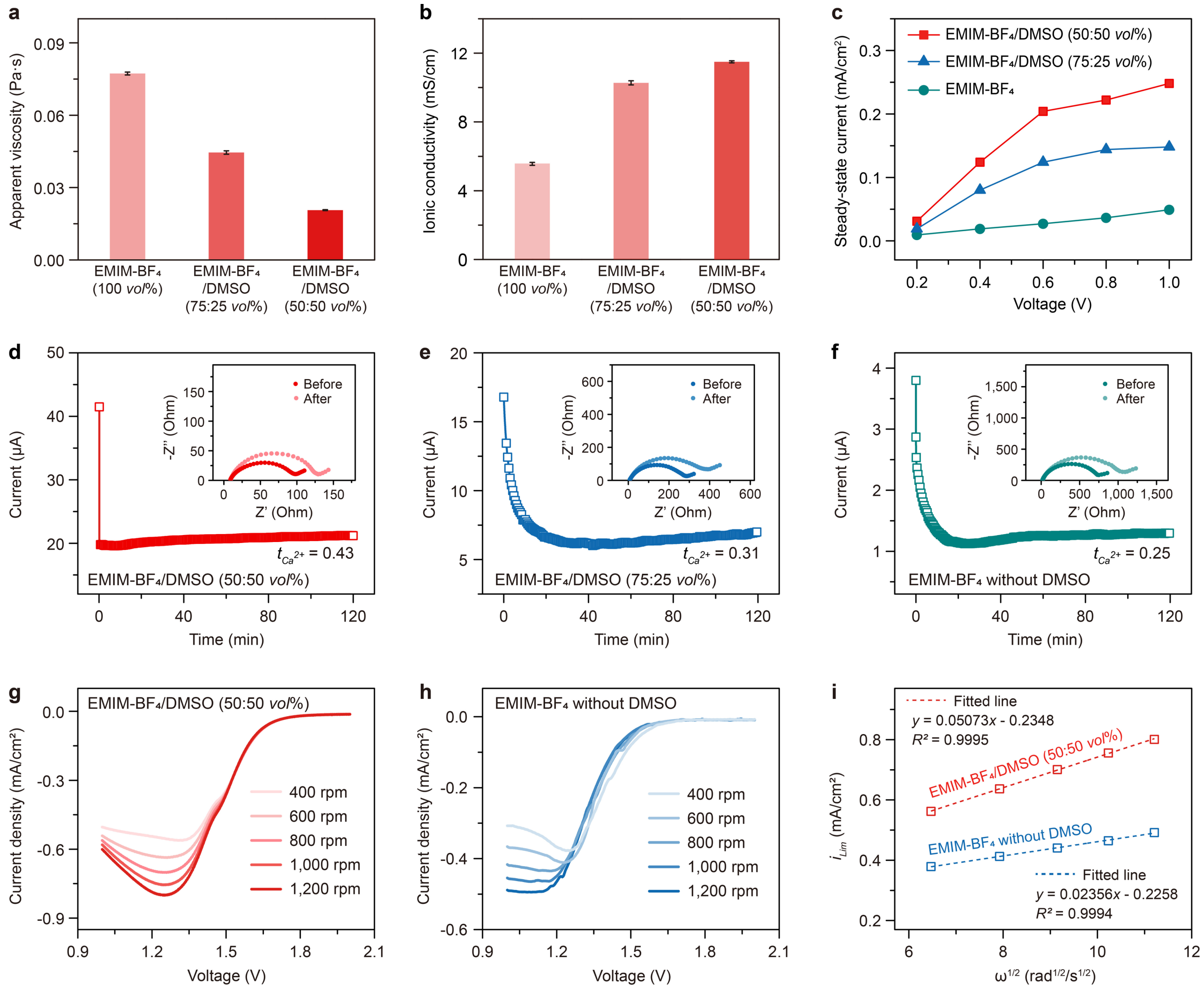

Extended Data Fig. 6 | Properties of the optimized electrolyte containing DMSO. **a**, Dependence of apparent viscosity on the electrolyte formula containing different volume ratio of DMSO, demonstrating that the electrolyte of EMIM-BF_4/DMSO (50:50 *vol*%) has the lowest apparent viscosity. **b**, Dependence of ionic conductivity on the electrolyte formula containing different volume ratio of DMSO, showing that the electrolyte of EMIM-BF_4/DMSO (50:50 *vol*%) has the highest ionic conductivity (11.5 mS/cm). **c**, Steady-state current density of electrolytes containing different volume ratio of DMSO upon varying applied polarization potentials. The electrolyte of EMIM-BF_4/DMSO (50:50 *vol*%) demonstrates the comparably higher steady-state current densities, pointing to the facilitated Ca^{2+} transportation. **d**–**f**, Potentiostatic polarization curves of the EMIM-BF_4/DMSO (50:50 *vol*%) electrolyte (**d**), EMIM-BF_4/DMSO (75:25 *vol*%) electrolyte (**e**), and EMIM-BF_4 electrolyte without DMSO (**f**). Inset, corresponding Nyquist plots of the electrolyte. Among the various electrolytes, our optimized electrolyte (**d**) has the highest Ca^{2+} transference number ($t_{Ca^{2+}} = 0.43$). **g**, **h**, Linear sweep voltammetry curves of the O_2 reduction reaction in electrolytes with DMSO (EMIM-BF_4/DMSO, 50:50 *vol*%, in **g**) and without DMSO (only EMIM-BF_4, in **h**) at a scan rate of 100 mV/s with rotating disc electrode rotation rates from 400 to 1,200 rpm and an increment of 200 rpm. The comparably higher limiting current densities in the electrolytes with DMSO (EMIM-BF_4/DMSO, 50:50 *vol*%) indicates the improved O_2 reduction reaction kinetics by the introduction of DMSO. The clear observation of O_2 reduction at about 1.5 V originates from the maximized exposure of working electrode to the continuously applied O_2 flux. **i**, The fitted linear Levich plots of the limiting current density (O_2 reduction reaction) *versus* the square root of rotation rate ($\omega^{1/2}$), deducing a higher O_2 diffusion coefficient of 1.69×10^{-6} cm²/s in the electrolyte with DMSO (EMIM-BF_4/DMSO, 50:50 *vol*%) than 4.47×10^{-7} cm²/s in the electrolyte without DMSO. Error bars represent the standard deviations of the results from five samples.

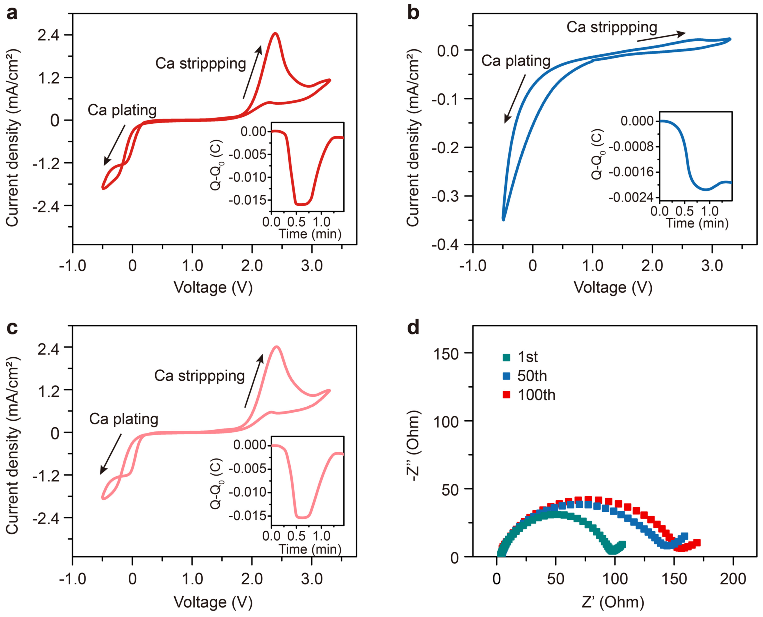

Extended Data Fig. 7 | Electrochemical performance of Ca metal anode in electrolytes with and without DMSO. a, Cyclic voltammogram of Ca plating/stripping in electrolyte with DMSO (EMIM-BF$_4$/DMSO (50:50 *vol*%)). Scan rate, 100 mV/s. Inset, passed charge during plating/stripping from the cyclic voltammogram. **b**, Cyclic voltammogram of Ca plating/stripping in electrolyte without DMSO (EMIM-BF$_4$). Scan rate, 100 mV/s. Inset, passed charge during plating/stripping. **c**, Cyclic voltammogram of Ca plating/stripping in electrolyte with DMSO (EMIM-BF$_4$/DMSO (50:50 *vol*%)) in the presence of O$_2$ shows similar reversibility compared with that without O$_2$ (**a**). Scan rate, 100 mV/s. Inset, passed charge during plating/stripping from the cyclic voltammogram. **d**, Nyquist plots of the symmetric battery after the 1st, 50th, and 100th Ca plating/stripping cycles.

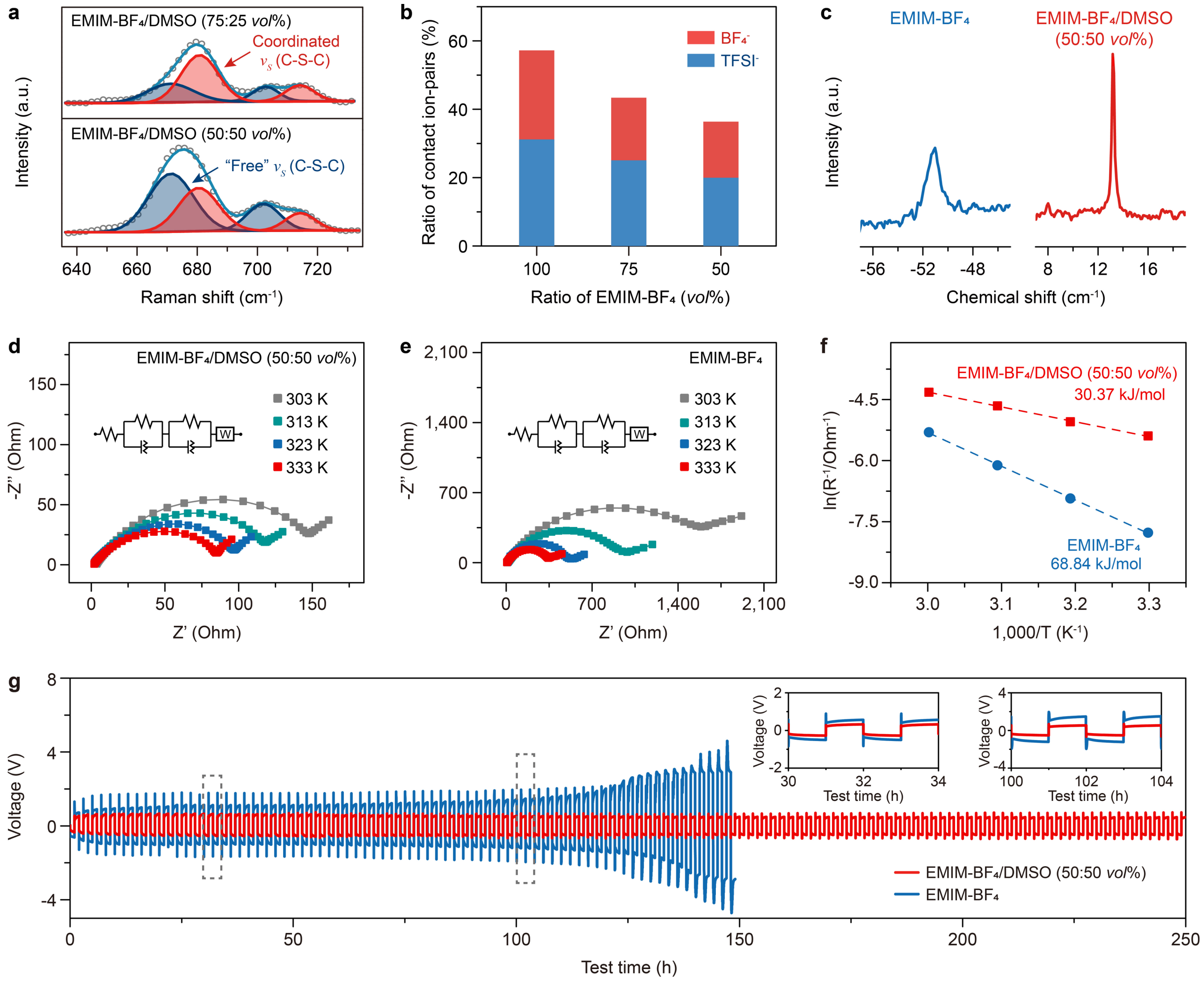

Extended Data Fig. 8 | Improved Ca^{2+} de-solvation and Ca plating/stripping. **a**, Raman spectra of the electrolytes with different volume ratio of DMSO, suggesting the coordination of DMSO and Ca^{2+}. **b**, Percentage of Ca^{2+}-coordinated BF$_4^-$/TFSI$^-$ as determined by the ratio between the peak area of coordinated species and the total peak area from the Raman spectra. DMSO effectively reduces Ca^{2+}-coordinated BF$_4^-$/TFSI$^-$. **c**, ^{43}Ca NMR spectra of electrolytes with DMSO (EMIM-BF$_4$/DMSO, 50:50 *vol*%) and without DMSO (only EMIM-BF$_4$) have different chemical shifts and shapes, suggesting that DMSO relieves the Ca^{2+} coordination by BF$_4^-$/TFSI$^-$ anions. **d**, **e**, Temperature-dependent Nyquist plots of symmetric batteries using the electrolytes with DMSO (EMIM-BF$_4$/DMSO, 50:50 *vol*%, in **d**) and without DMSO (only EMIM-BF$_4$, in **e**). **f**, Arrhenius plots of the resistance corresponding to Ca^{2+} de-solvation in electrolytes with DMSO (red) and without DMSO (blue), suggesting that the introduced DMSO can reduce the Ca^{2+} de-solvation energy barrier. **g**, Voltage curves of Ca||Ca symmetric cells using electrolytes with DMSO (EMIM-BF$_4$/DMSO, 50:50 *vol*%) and without DMSO (only EMIM-BF$_4$) at a current density of 0.2 mA/cm^2 and an areal capacity of 0.2 mAh/cm^2. Inset, the enlarged voltage curves.

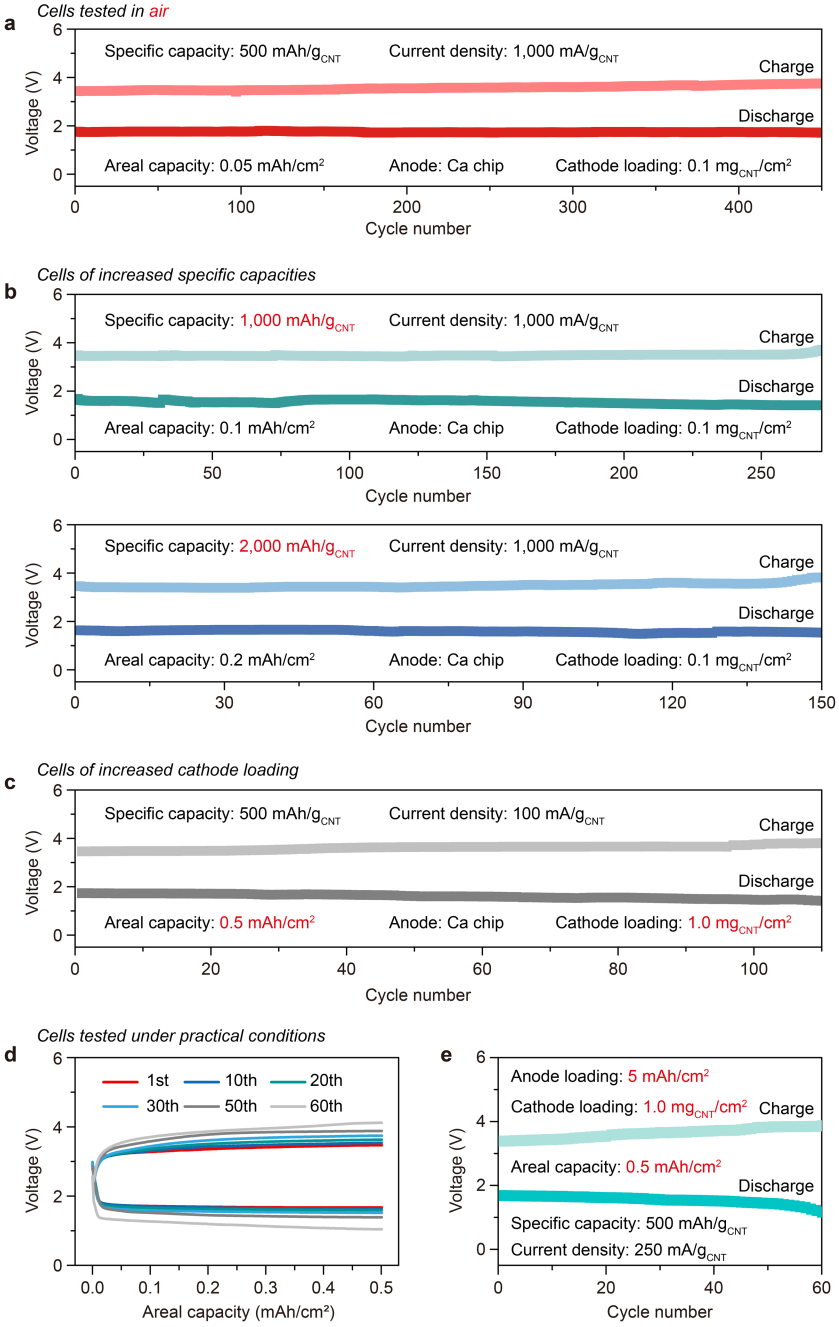

Extended Data Fig. 9 | Electrochemical performance of Ca-O$_2$ batteries under practical conditions. a, Discharge and charge voltage plateaus of the Ca-O$_2$ battery tested in air show a stable cycling performance for over 450 cycles at a current density of 1 A/g and a specific capacity of 500 mAh/g. **b**, Discharge and charge voltage plateaus at 1 A/g and specific capacity at 1 Ah/g of the Ca-O$_2$ battery display stable cycling for over 270 cycles (top). Discharge and charge voltage plateaus at 1 A/g and specific capacity at 2 Ah/g of the Ca-O$_2$ battery are stable for over 150 cycles (bottom). **c**, Discharge and charge voltage plateaus of the Ca-O$_2$ battery with a CNT cathode mass loading of 1 mg/cm^2 show a stable cycling performance for over 100 cycles at a current density of 100 mA/g and a specific capacity of 500 mAh/g (*i.e.*, areal capacity of 0.5 mAh/cm^2). **d**, Discharge and charge voltage curves of a Ca-O$_2$ battery based on a thin metallic Ca anode (5 mAh/cm^2) at an areal capacity of 0.5 mAh/cm^2 and a current density of 0.25 mA/cm^2. **e**, Evolution of the discharge and charge plateaus in **d**.

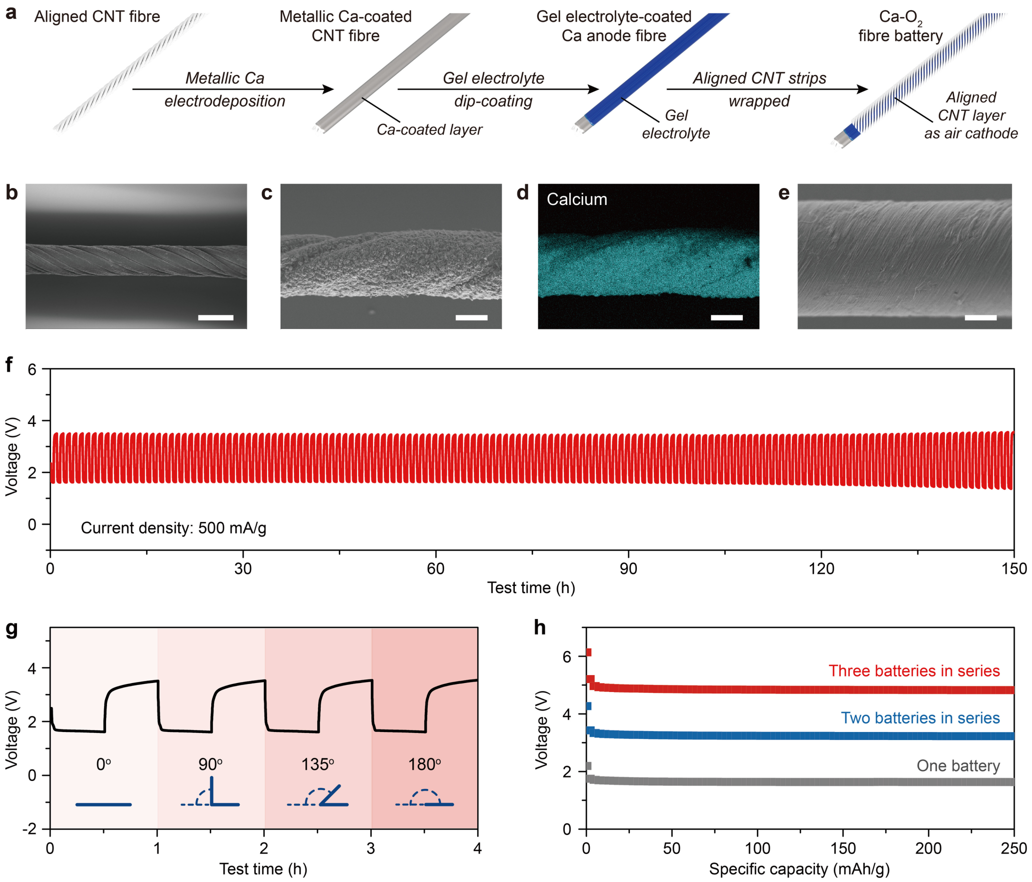

Extended Data Fig. 10 | Fabrication and electrochemical performances of fibre Ca-O_2 batteries. a, Schematic illustration to the preparation procedures of the flexible fibre Ca-O_2 batteries. **b**, SEM image of aligned CNT fibre as the current collector for fibre batteries. Scale bar, 50 µm. **c**, **d**, SEM and elemental mapping images of metallic Ca-coated fibre anode, respectively. Scale bars, 100 µm. **e**, SEM image of the fibre Ca-O_2 battery wrapped by a layer of aligned CNT as the air cathode. Scale bar, 100 µm. **f**, Flexible fibre Ca-O_2 battery showing a cycle life over 100 h at a current density of 500 mA/g and a specific capacity of 250 mAh/g. **g**, Galvanostatic discharge/charge curves of the fibre Ca-O_2 battery under increasing bending angles (0 to 180°). Fibre batteries remain stable when deformed. **h**, Discharge curves of fibre Ca-O_2 batteries connected in series.

Extended Data Table 1 | Atomic percentage (*at*%) of the elements observed in XPS spectra of Ca deposits in anode disassembled from our Ca-O_2 batteries at different sputtering time

Element*	0 s (*at*%)	120 s (*at*%)	240 s (*at*%)
Carbon	39.71	24.22	20.28
Calcium	8.28	35.63	46.94
Fluorine	22.19	17.58	15.93
Sulfur	2.79	2.43	1.17
Boron	7.24	5.81	4.33
Nitrogen	4.28	3.3	2.41
Oxygen	15.51	11.03	8.94

(footnote: *Samples were prepared in the glovebox and transferred into the instrument through a vacuum transfer vessel).

Extended Data Table 2 | The parameters measured by potentiostatic polarization and electrochemical impedance spectroscopy for calculating the Ca^{2+} transference number

Electrolyte	Applied potential (ΔV, mV)	Initial current (I_o, μA)	Steady-state current (I_{ss}, μA)	Initial resistance (R_o, Ω)	Steady-state resistance (R_{ss}, Ω)	Ca^{2+} transference number* ($t_{Ca^{2+}}$)
EMIM-BF_4/DMSO (50:50 *vol*%)	10	41.51	21.20	87.3	116.0	0.43
EMIM-BF_4/DMSO (75:25 *vol*%)	10	16.70	7.05	280.3	384.6	0.31
EMIM-BF_4	10	3.80	1.13	716.0	1074.1	0.25

(footnote: *Measured in the symmetric coin cell consisting of two Ca chips).